On the appearance of internal wave attractors due to an initial or parametrically excited disturbance

J A N I S B A J A R S[1]†, **J A S O N F R A N K**[1]
A N D L E O R. M. M A A S[2]

[1]Centrum Wiskunde & Informatica, P.O. Box 94079, 1090 GB Amsterdam, the Netherlands
[2]Royal Netherlands Institute for Sea Research, P.O. Box 59, 1790 AB Texel, the Netherlands

In this paper we solve two initial value problems for 2D internal gravity waves. The waves are contained in a uniformly-stratified, square-shaped domain whose side walls are tilted with respect to the direction of gravity. We consider several disturbances of the initial stream function field and solve both for its free evolution and for its evolution under parametric excitation. We do this by developing a structure-preserving numerical method for internal gravity waves in a 2D stratified fluid domain. We recall the linearized, inviscid Euler-Boussinesq model, identify its Hamiltonian structure, and derive a staggered finite difference scheme that preserves this structure. For the discretized model, the initial condition can be projected onto normal modes whose dynamics is described by independent harmonic oscillators. This fact is used to explain the persistence of various classes of wave attractors in a freely evolving (i.e. unforced) flow. Under parametric forcing, the discrete dynamics can likewise be decoupled into Mathieu equations. The most unstable resonant modes dominate the solution, forming wave attractors.

---

1. Introduction

Internal gravity waves in stratified fluids retain their frequency and consequently also their angle with respect to gravity upon reflection from an inclined boundary. Waves do change their wavelength and become focused or defocused when reflecting from plane, inclined surfaces. Laboratory experiments confirm that when a container filled with a uniformly stratified fluid is excited vertically or horizontally, internal gravity waves appear that become focused when reflecting from a sloping wall and converge towards a limit cycle, a so called wave attractor (Maas & Lam 1995; Maas *et al.* 1997; Hazewinkel *et al.* 2008). Energy propagates along the straight lines of the attractor, which are normal to the direction of phase propagation. Understanding the behavior of internal waves in bounded domains may be important for explaining the mixing processes in ocean basins and lakes and has relevance to astrophysics and fluid dynamics in general (Bühler & Holmes-Cerfon 2011).

The ansatz of a time-periodic, single frequency (monochromatic) solution to the linearized internal gravity wave equations yields a wave equation in space with Dirichlet
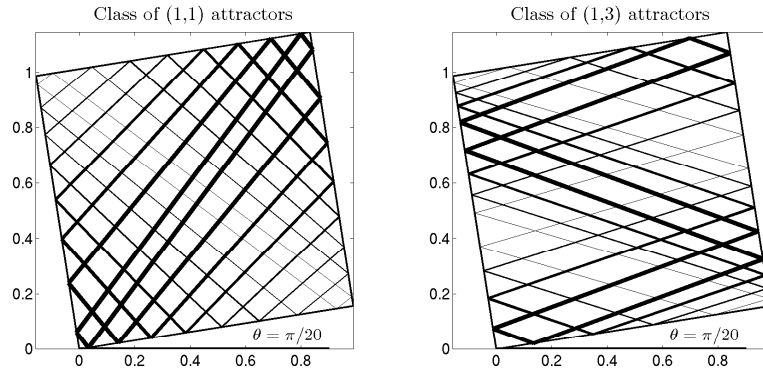
FIGURE 1. Limit cycle wave attractors corresponding to a discrete set of frequencies from the respective continuum range. Different line thicknesses correspond to distinct wave attractors. Left: class of $(1, 1)$ attractors. Right: class of $(1, 3)$ attractors.
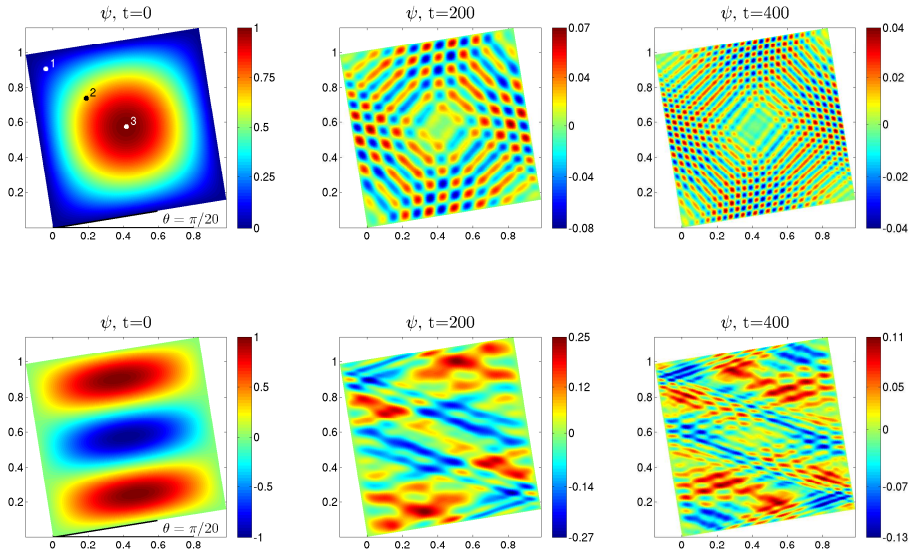

FIGURE 2. Evolution of the stream function in time from two distinct Fourier mode initial conditions.

boundary conditions. This makes the problem quite unusual, as it is ill-posed due to nonuniqueness. The problem can be solved exactly using the method of characteristics or through a regularization technique (Swart *et al.* 2007). Via the method of characteristics one can study the limit behavior of reflecting rays in bounded domains. The most generic asymptotic solution is an attractor, which is a finite closed orbit of rays within the domain. The particular structure of internal gravity wave attractors in a tilted square domain depends on: the rotation angle of the square θ, the wave frequency ω and the stratification frequency N_f. A family of wave attractors is characterized by the number of reflections of the attractors with the boundary. By symmetry considerations, an attractor must reflect an equal number n times with the top and bottom domain boundaries, and

an equal number m times with the left and right boundaries. Such an attractor is called an (n, m)-attractor. In Figure 1 shows a sample of the geometries from the classes of (1,1)- and (1,3)-attractors in a tilted square domain (see §2).

Due to the ill-posedness of the monochromatic wave problem, we are motivated to study the initial value problem for internal gravity waves in a confined region. Alternatively, one could introduce viscosity, which regularizes the monochromatic wave problem, allowing for its approximate analytical solution (Ogilvie 2005). Lighthill (1996) considered the initial value problem for the evolution of a localized disturbance in an unbounded domain, deriving the dispersion relation and noting that vortical structures remain stationary after internal gravity waves have propagated away horizontally. In this paper we study internal waves in a stratified fluid filling a domain with solid walls, so that wave motion is trapped inside. We consider the simplest case that admits wave attractors: perturbations to a linearly stratified inviscid fluid, either freely evolving or parametrically excited. To guarantee that viscous effects play no role, we construct a numerical discretization that conserves total energy and symmetry in the absence of forcing and study two idealized theoretical configurations: freely evolving (i.e. unforced) flow, and parametrically excited flow. We proceed with a normal mode analysis of the discrete model. For the first configuration, we analyze the unforced initial boundary value problem, to show how linear dynamics is partitioned into normal modes for different classes of initial conditions. Figure 2 illustrates the free evolution from Fourier modes with wave numbers $(1, 1)$ and $(1, 3)$, respectively. Evident in the plots at later times, we observe structures reminiscent of the full class of $(1, 1)$- and $(1, 3)$-attractors, suggesting a relationship between the Fourier modes and attractor geometries, for which we give some motivation. For the second configuration, the normal mode analysis reveals that the flow may be decomposed into independent Mathieu equations, and that those modes whose associated frequencies lie within the resonance zones (Arnold tongues) will be amplified, forming a wave attractor.

It is important to note that the existence of a complete normal mode decomposition for the discretized model contrasts sharply with the continuum model, for which the eigen-spectrum is continuous and no such decomposition exists (Maas 2005). The continuous spectrum for the continuum model actually implies the existence of an uncountable infinity of time-periodic solutions, corresponding to the arbitrary definition of the boundary condition on the fundamental intervals, that we will discuss. For the discretized system, the finite basis of normal modes are precisely the time-periodic solutions. The complete normal mode decomposition for the discrete model is also non-robust with respect to viscous perturbation of the system. For the forced system with viscosity, the normal mode basis becomes time dependent, meaning the solution cannot be decomposed into scalar problems.

The paper is organized as follows: In §2 we recall the 2D linear hydrostatic inviscid Euler-Boussinesq equations which govern internal gravity waves in stratified fluids, discuss monochromatic solutions in a tilted square domain, and review the Hamiltonian structure. In §3 we describe a structure-preserving finite difference discretization on the tilted square and present the normal mode analysis of the discretized model in the unforced and forced cases. Using the symmetries of the discrete differential operators we show that in both cases the dynamics may be projected onto a constant in time basis of normal modes, such that they entirely decompose into independent scalar problems: harmonic oscillators in the unforced case or Mathieu equations in the forced case. In §4 we present numerical experiments of the unforced and forced models. We observe that an (n, m) Fourier mode initial condition projects mostly onto the range of the associated (n, m)-attractor, explaining the similarities of Figures 1 and 2. For the forced model we

observe that if the initial condition has a nontrivial projection onto normal modes with amplified Mathieu dynamics, a wave attractor will emerge. Conclusions are summarized in §5.

2. Euler-Boussinesq equations

2.1. *Internal gravity wave equations*

We consider a vertical slice domain $D \subset \mathbb{R}^2$ with boundary ∂D and Cartesian coordinates $\boldsymbol{x} = (x, z)$, where z is directed antiparallel to the direction of gravity, **g**. We decompose the fluid density field and the pressure field as follows:

$$\rho(x, z, t) = \rho_0 + \bar{\rho}(z) + \rho'(x, z, t), \qquad p(x, z, t) = \bar{p}(z) + p'(x, z, t),$$

where ρ_0 is an average constant mean density and $\bar{\rho}(z)$ is a mean static density stratification, i.e. a monotonically decreasing function of z. The sum $\rho_0 + \bar{\rho}(z)$ defines a stable background density field in a hydrostatic balance with the pressure field $\bar{p}(z)$:

$$\partial_z \bar{p} = -g(\rho_0 + \bar{\rho}(z)),$$

where g is the gravitational acceleration. The quantities $\rho'(x, z, t)$ and $p'(x, z, t)$ are small amplitude perturbations about the (steady state) background density and pressure fields.

In geophysical and astrophysical fluid dynamics it is common to treat the density field distinctly, defining both an 'inertial mass' and a 'gravitational mass'. The Boussinesq approximation consists in assuming a constant density value ρ_0 for the inertial mass in the momentum equation (from which the density may be consequently removed), while maintaining the full density ρ for the gravitational mass. We enforce the inequality $|\rho'| < |\bar{\rho}(z)| \ll \rho_0$ to justify the Boussinesq approximation. Such flows are termed 'buoyancy-driven'. The background stratification defines a stratification frequency, N_f, (Brunt-Väisälä frequency), where $N_f^2 = -g\rho_0^{-1} d\bar{\rho}/dz$. In the following we assume that N_f is a constant, i.e., the fluid is linearly stratified in the background density.

Wave focusing occurs when a boundary of the domain is inclined with respect to gravity. For this reason we assume the domain D is rotated through an angle $0 \leqslant \theta \leqslant \pi/4$. With the above considerations in mind, the inviscid linear Euler-Boussinesq equations describing the propagation of perturbations in this rotated frame read:

$$\partial_t \boldsymbol{u} = -\nabla \hat{p} + b\hat{\boldsymbol{k}}(\theta), \tag{2.1}$$

$$\partial_t b = -N_f^2 \boldsymbol{u} \cdot \hat{\boldsymbol{k}}(\theta), \tag{2.2}$$

$$\nabla \cdot \boldsymbol{u} = 0, \tag{2.3}$$

$$\boldsymbol{u} \cdot \hat{\boldsymbol{n}} = 0 \quad \text{on} \quad \partial D, \tag{2.4}$$

where $\boldsymbol{u} = (u, w)$ is a velocity field in the x and z direction respectively (now *tilted* relative to the original direction), $\hat{p} = \rho_0^{-1} p'$ is scaled pressure with respect to the mean constant density, $b = -g\rho' \rho_0^{-1}$ is the buoyancy, $\hat{\boldsymbol{k}}(\theta) = (\sin\theta, \cos\theta)$ is the unit vector in the direction opposite to gravity and $\hat{\boldsymbol{n}}$ is the unit outward normal to the boundary ∂D.

In two-dimensions it is convenient to consider the stream function formulation of the Euler-Boussinesq equations (2.1)–(2.4). The divergence-free condition (2.3) allows us to define a stream function ψ on D such that

$$u = -\partial_z \psi, \qquad w = \partial_x \psi.$$

By taking the curl of the momentum equations (2.1) we eliminate the pressure from (2.1), obtaining the 2D linear inviscid Euler-Boussinesq equations in stream function

formulation:

$$\partial_t q = -\partial_x b \cos\theta + \partial_z b \sin\theta, \tag{2.5}$$

$$\partial_t b = -N_f^2(\partial_x \psi \cos\theta - \partial_z \psi \sin\theta), \tag{2.6}$$

$$q = -\Delta\psi, \tag{2.7}$$

$$\psi = 0 \quad \text{on} \quad \partial D, \tag{2.8}$$

where $q = \partial_z u - \partial_x w$ is vorticity.

The model (2.5)–(2.8) is a system of partial differential equations that conserve total energy:

$$\mathcal{H} = \frac{1}{2}\int_D \nabla\psi \cdot \nabla\psi + \frac{1}{N_f^2}b^2 \, d\boldsymbol{x}, \tag{2.9}$$

equal to the sum of kinetic and potential energies.

2.2. *Forcing*

Wave attractors are generated by periodically forcing a stratified fluid in domain with inclined boundaries. In the ocean, the forcing is primarily tidal forcing. In laboratory experiments (Maas *et al.* 1997; Lam & Maas 2008), wave attractors were generated by vertically oscillating a container with a sloping wall. To incorporate such *parametric excitation* (McEwan & Robinson 1975) equation (2.5) is modified by multiplication with a time dependent function $\alpha(t)$ to obtain:

$$\partial_t q = \alpha(t)(-\partial_x b \cos\theta + \partial_z b \sin\theta).$$

An alternative approach is *external excitation*, for which time dependent terms may be added to (2.5) and (2.6), (Ogilvie 2005, see), or by means of boundary forcing (Grisouard *et al.* 2008).

Vertical oscillation of the container can be viewed as time-dependent modulation of the gravitational parameter g, which originally enters the momentum equation, and should thus be present only in the vorticity equation (2.5). Hence, we can realize this kind of forcing as parametric excitation with

$$\alpha(t) = 1 - \epsilon\cos(2\bar{\omega}t) \tag{2.10}$$

where ϵ is a positive constant smaller than one and $2\bar{\omega}$ is the forcing frequency.

2.3. *Dispersion properties of internal gravity waves*

Consider a time periodic solution

$$\psi(x,z,t) = \Psi(x,z)e^{-i\omega t}, \qquad b(x,z,t) = B(x,z)e^{-i\omega t}.$$

Substituting the above ansatz into (2.5)–(2.7), eliminating B and taking $\theta = 0$ without loss of generality yields

$$\partial_{zz}\Psi - \frac{(N_f^2 - \omega^2)}{\omega^2}\partial_{xx}\Psi = 0, \tag{2.11}$$

which is recognized as a wave equation for the scalar state variable Ψ. In other words, internal gravity waves are spatially governed by the wave equation. Substituting the plane wave

$$\Psi(x,z) = a\exp(i(\kappa_x x + \kappa_z z)),$$

into (2.11), where a is the amplitude and κ_x and κ_z are wave numbers, yields the dispersion relation

$$\omega^2 = N_f^2 \frac{\kappa_x^2}{\kappa_x^2 + \kappa_z^2} = N_f^2 \cos^2 \phi, \tag{2.12}$$

the last equality of which follows from the polar coordinate description of the wave number vector $\boldsymbol{\kappa} = |\boldsymbol{\kappa}|(\cos\phi, \sin\phi)$ where $|\boldsymbol{\kappa}|$ is the wave number magnitude and ϕ is the phase angle. Hence, $\omega^2 \leqslant N_f{}^2$ and the frequencies of internal gravity waves are bounded by the stratification frequency N_f. It is also apparent that the wave frequency is independent of the wave number magnitude and depends only on its angle ϕ. Consequently an incident wave retains its propagation direction upon reflection from a plane surface independent of the slope of the surface, leading to monoclinical (single-angled) waves. A wave does, in general, change its wavelength and can become focused or defocused upon reflection from an inclined boundary. It is well known that the wave phase travels in the phase velocity direction $\boldsymbol{c_p} = \omega\boldsymbol{\kappa}/|\boldsymbol{\kappa}|^2$ and wave packet energy is transported by the group velocity $\boldsymbol{c_g} = \nabla_{\boldsymbol{\kappa}}\omega$, Whitham (1974). The internal wave group velocity vector $\boldsymbol{c_g}$ and phase velocity vector $\boldsymbol{c_p}$ are mutually perpendicular, i.e., $\boldsymbol{c_g} \cdot \boldsymbol{c_p} = 0$. Hence internal waves propagate energy parallel to the wave crests and troughs (i.e. along these).

2.4. *Monochromatic wave solutions in a tilted square*

The wave equation (2.11) with Dirichlet boundary conditions (2.8) is formally an ill-posed problem (Swart *et al.* 2007). One not only finds a trivial solution $\psi \equiv 0$, but there exist infinitely many solutions. For example, the hyperbolic wave equation (2.11) can be solved on a non-inclined ($\theta = 0$) rectangular domain $(x, z) \in [0, 1] \times [0, \ell]$ by separation of variables. The function

$$\Psi = A_{n,m} \sin(n\pi x) \sin(m\pi z/\ell)$$

satisfies the hyperbolic equation (2.11) provided that

$$\ell = \sqrt{\frac{\omega^2}{N_f^2 - \omega^2}} \frac{m}{n}. \tag{2.13}$$

Replacing (n, m) in (2.13) by (jn, jm) leaves ℓ unchanged, and for integer j, Ψ still vanishes at the boundaries. Therefore there are infinitely many solutions to the wave equation (2.11), resulting in the ill-posedness.

The general solution of the wave equation is given by

$$\Psi(x, z) = f(x - \gamma z) - g(x + \gamma z), \qquad \gamma = \sqrt{\frac{N_f^2 - \omega^2}{\omega^2}}$$

for arbitrary functions f and g that are invariant along characteristics $x \pm \gamma z = const$. For zero Dirichlet boundary conditions for the stream function (2.8) it follows that on the boundary the value of f of a reflecting characteristic equals that of g on the incident characteristic, $f \equiv g$. Thus we can compute the stream function at any given point by following the characteristics until they intersect the boundary on an interval where the function $f = g$ has been prescribed. Thus the problem reduces to identifying a minimal set of distinct intervals, the so called fundamental intervals, on the boundary where the functions f and g may be prescribed, (see Maas & Lam 1995).

For this paper we will study internal waves in a tilted square domain. In the tilted unit square the sequence of successive reflecting characteristics exhibits different behavior depending on the angle of tilt and stratification and forcing frequencies. In the subcritical

case all characteristics approach asymptotically either the square's upper left and lower right corners, or the square's lower left and upper right corners. This occurs when the characteristic slope is either larger or smaller than the inclination of both sets of boundaries, i.e of the bottom/surface and left/right walls. In the supercritical case one can distinguish an additional three subtypes of limit behavior: periodic, ergodic and limit cycle (John 1941; Kopecz 2006). In the periodic case the web of boundary intersection points consists only of a finite number of elements, and the characteristic orbit through every point is periodic. In the ergodic case, for each starting value the characteristic orbit eventually passes arbitrarily close to every other point in the domain (the stream function is then necessarily constant, implying no flow). The most generic case of limit behavior of the reflecting characteristics is a limit cycle, i.e., a periodic orbit that attracts a neighborhood of itself. The periodic orbits are characterized by the number of boundary intersections they have. Due to the symmetry we say that attractor (n, m) has n intersections with the boundary on the upper side of the square and m intersections on the left side of the square. The overall number of attractor intersections with the boundary is called the attractor's period. In the unit square domain all attractors are global.

The choice of the fundamental intervals on the boundary and the functions prescribed on it is not unique. In the subcritical case it is sufficient to prescribe only one interval between two successive characteristic intersections on the boundary. In the ergodic case the solution may be prescribed at only one point on the boundary yielding the trivial solution $\psi \equiv 0$ of the wave equation (2.11) due to the zero Dirichlet boundary conditions (2.8). For the periodic and attractor cases one must prescribe one or two intervals on one of the square's boundaries, respectively. For a complete discussion see Maas & Lam (1995).

We take a closer look at periodic solutions and limit cycles. The experimental variables are the wave frequency ω, stratification frequency N_f and a rotation angle of the square θ. In the periodic solution regime, all orbits correspond to odd-even pairs $(2n, 2m + 1)$ or $(2n + 1, 2m)$, implying that focusing of characteristics is offset by an equal amount of defocusing. But the periodic regime is non-robust with respect to perturbations in domain geometry. In the tilted square domain these solutions occur only for a discrete set of frequencies. In contrast the limit cycle attractors persist over a continuous range of frequencies, hence are robust with respect to frequency perturbations. In the simplest periodic case the characteristic emanating from, say, the square lower left corner will intersect the lower right corner after $2n$ successive intersections at the top of the square or will intersect the upper left right corner after $2m$ successive intersections at the right side of the square. In both such situations we have analytic expressions relating the wave frequency ω, stratification frequency N_f and rotation angle of the square θ:

$$\cot\left(\theta + \tan^{-1}\sqrt{\frac{\omega^2}{N_f^2 - \omega^2}}\right) - \cot\left(\theta - \tan^{-1}\sqrt{\frac{\omega^2}{N_f^2 - \omega^2}}\right) = \frac{1}{n},$$

$$\tan\left(\theta + \tan^{-1}\sqrt{\frac{\omega^2}{N_f^2 - \omega^2}}\right) - \tan\left(\theta - \tan^{-1}\sqrt{\frac{\omega^2}{N_f^2 - \omega^2}}\right) = \frac{1}{m},$$

respectively. Hence these periodic solutions are indicated as $(2n, 1)$ and $(1, 2m)$ with periods $2(2n + 1)$ and $2(2m + 1)$, respectively.

Figure 3 illustrates the parameter space ω/N_f versus θ. The black bold line separates subcritical and supercritical regimes. Periodic solutions $(2n, 1)$ and $(1, 2m)$ are indicated in Figure 3(a) with blue lines. Note that for a given rotation angle θ, the periodic solutions

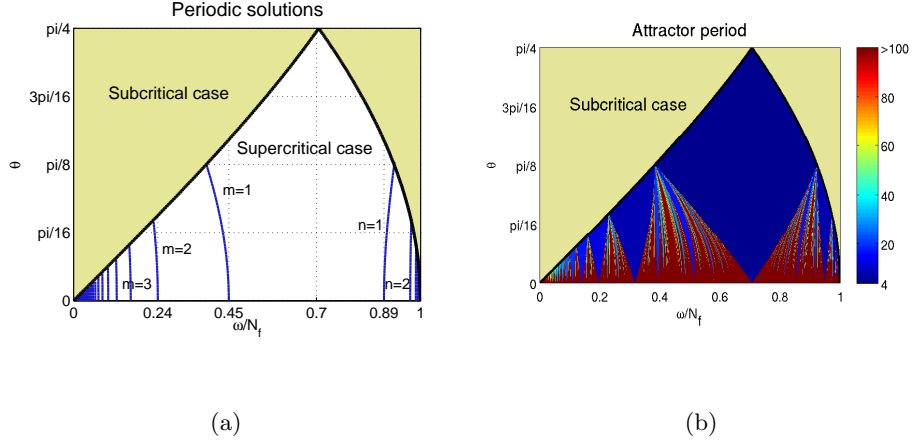(a)   (b)

FIGURE 3. Left: periodic solutions $(2n,1)$ and $(1,2m)$ indicated with numbers $n = 1, 2, \ldots$ and $m = 1, 2, 3, \ldots$, respectively. Right: attractor period.
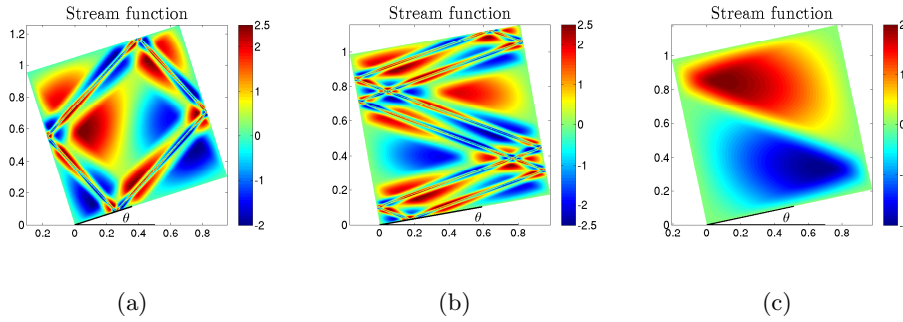

(a)   (b)   (c)

FIGURE 4. Left: stream function and attractor (1,1), $\theta = 7\pi/72$ and $\omega/N_f = 0.74$. Middle: stream function and attractor (1,3), $\theta = \pi/18$ and $\omega/N_f = 0.34$. Right: stream function and periodic solution $(1,2)$, $\theta = \pi/15$ and $\omega/N_f = 0.43$.

correspond to discrete values of ω/N_f. Limit cycle solutions are indicated in Figure 3(b), where the color denotes the period of the attractor.

Figure 4 shows solutions of the monochromatic wave equation (2.11) for the $(1,1)$ and $(1,3)$ attractor cases and for the $(1,2)$ periodic case, for specific value of θ and ω/N_f. In Figures 4(a) and 4(b) we show two typical members from the respective continuum ranges of limit cycle solutions. In both cases one can observe a self-similar structure approaching the attractor. The solutions were constructed using the method of characteristics; on the fundamental intervals we prescribe two cosines with an offset at the chosen intervals. For a square-shaped attractor in a trapezoidal geometry a free wave solution was computed analytically, possessing a logarithmic self similar Fourier spectrum (Maas 2009).

3. Numerical discretization and linear analysis

In this section we describe our discrete model equations and show that in the special case of linear inviscid flow, the dynamics decouples into scalar oscillators.

3.1. *Fourier analysis of the continuum model, non-tilted*

For a non-tilted square domain ($\theta = 0$), the initial boundary value problem for the linear Euler-Boussinesq equations (2.5)–(2.8) with initial conditions $\psi_0(x, z)$ and $b_0(x, z)$ and zero Dirichlet boundary conditions (2.8) can be solved analytically using separation of variables. The solution is

$$\psi(x, z, t) = \sum_{n,m=1}^{\infty} \psi_{n,m}(x, z)\frac{d}{dt}T_{n,m}(t), \qquad b(x, z, t) = -N_f^2 \sum_{n,m=1}^{\infty} \partial_x \psi_{n,m}(x, z)T_{n,m}(t),$$

(3.1)

where $\psi_{n,m}(x, z) = \sin(n\pi x)\sin(m\pi z)$ are Fourier modes on the unit square, i.e. the eigenfunctions of the operators ∂_{xx} and ∂_{zz} under the given boundary conditions, and $T_{n,m}$ is a solution to the simple harmonic oscillator equation

$$\frac{d^2}{dt^2}T_{n,m} = -\omega_{n,m}^2 T_{n,m}, \qquad \omega_{n,m}^2 = N_f^2 \frac{n^2}{n^2 + m^2},$$

(3.2)

with the frequencies given by the dispersion relation (2.12).

The total energy functional (2.9) of the general solution in the form (3.1) is

$$\mathcal{H} = \frac{\pi}{8} \sum_{n,m=1}^{\infty} \left[(n^2 + m^2) \left(\frac{d}{dt}T_{n,m} \right)^2 + N_f^2 n^2 T_{n,m}^2 \right] = \sum_{n,m=1}^{\infty} \mathcal{H}_{n,m},$$

where for each (n, m), the term in square brackets, $\mathcal{H}_{nm}$, is the independently conserved Hamiltonian of (3.2). Note that there is no coupling between wave numbers. The initial conditions may be projected onto the Fourier modes, but each mode evolves independently, and there is no energy exchange between modes.

The situation for $\theta \neq 0$ is very different. The initial boundary value problem (2.5)–(2.8) cannot be solved analytically by the method of separation of variables as it was done above. The eigenfunctions in the tilted case correspond to the ill-posed solutions of (2.11), and have no simple representation. However, as we show in the next section, the numerical discretization does admit a normal mode analysis.

3.2. *Energy conserving numerical discretization and analysis*

Making use of the Hamiltonian structure of (2.5)–(2.8), we construct in Appendix A an energy preserving numerical discretization. Discretizing in space while leaving time continuous yields the following system of linear ordinary differential equations (cf. (A 11)–(A 13)):

$$-L\frac{d\boldsymbol{\psi}}{dt} = \alpha(t) \left(D_x^T M_z \boldsymbol{b} \cos\theta - D_z^T M_x \boldsymbol{b} \sin\theta \right),$$

(3.3)

$$\frac{d\boldsymbol{b}}{dt} = -N_f^2 (M_z^T D_x \boldsymbol{\psi} \cos\theta - M_x^T D_z \boldsymbol{\psi} \sin\theta),$$

(3.4)

where $\boldsymbol{\psi} \in \mathbb{R}^M$ and $\boldsymbol{b} \in \mathbb{R}^N$, $M < N$, are vectors containing the values of ψ and b at (staggered) grid positions, and the finite difference matrices M_x, M_z, D_x, D_z and L, defined in §A.1, represent discretized mean (M_*), difference (D_*) and Laplacian (L) operators. Here we introduced the factor $\alpha(t)$, that allows us to add forcing by means of parametric excitation.. Introducing the matrix $K = D_x^T M_z \cos\theta - D_z^T M_x \sin\theta$, this system can be written in matrix form

$$\begin{bmatrix} -L & 0 \\ 0 & I \end{bmatrix} \frac{d}{dt} \begin{pmatrix} \boldsymbol{\psi} \\ \boldsymbol{b} \end{pmatrix} = \begin{bmatrix} 0 & \alpha(t)K \\ -K^T & 0 \end{bmatrix} \begin{pmatrix} \boldsymbol{\psi} \\ \boldsymbol{b} \end{pmatrix}$$

(3.5)

By construction, when forcing is absent ($\alpha \equiv 1$) the discretization possesses a first integral, the discrete Hamiltonian H (A 8), which approximates the total energy (2.9), i.e.,

$$H = \frac{1}{2}\left(-\boldsymbol{\psi}^T L \boldsymbol{\psi} + \frac{1}{N_f^2}\boldsymbol{b}^T\boldsymbol{b}\right)\Delta x\,\Delta z. \qquad (3.6)$$

In Appendix B we derive the normal mode bases $X = (X_1, \ldots, X_M)$ and $Y = (Y_1, \ldots, Y_N)$, in which $\boldsymbol{\psi}$ and $\boldsymbol{b}$ are expressed as, cf. (B 7),

$$\boldsymbol{\psi} = X\tilde{\boldsymbol{\psi}}, \qquad \boldsymbol{b} = Y\tilde{\boldsymbol{b}}.$$

In the new basis, the system (3.5) decouples into M second order problems:

$$\frac{d^2}{dt^2}\tilde{\psi}_i = -\alpha(t)\omega_i^2\tilde{\psi}_i + \dot{\alpha}(t)\omega_i\tilde{b}_i, \qquad (3.7)$$

$$\frac{d^2}{dt^2}\tilde{b}_i = -\alpha(t)\omega_i^2\tilde{b}_i, \qquad (3.8)$$

for $i = 1, \ldots, M$, plus the trivial dynamics $\frac{d^2}{dt^2}\tilde{b}_i = 0$, $i = M+1, \ldots, N$.

When forcing is absent, $\alpha(t) \equiv 1$, the dynamics further decouples into $2M$ independent harmonic oscillators

$$\frac{d^2}{dt^2}\tilde{\psi}_i = -\omega_i^2\tilde{\psi}_i, \qquad \frac{d^2}{dt^2}\tilde{b}_i = -\omega_i^2\tilde{b}_i, \qquad i = 1, \ldots, M.$$

In particular the total energy can be expressed as the sum of the harmonic oscillator energies

$$H = \sum_{i=1}^{M} H_i^\psi + H_i^b, \qquad H_i^\psi = \frac{1}{2}\left[\left(\frac{d\tilde{\psi}_i}{dt}\right)^2 + \omega_i^2\tilde{\psi}_i^2\right], \quad H_i^b = \frac{1}{2}\left[\left(\frac{d\tilde{b}_i}{dt}\right)^2 + \omega_i^2\tilde{b}_i^2\right],$$

each of which is a conserved quantity.

Remark. In §2 we saw that there are infinitely many monochromatic wave solutions to the linearized Euler-Boussinesq equations, corresponding to an arbitrary specification of the solution on a fundamental interval. For the discretized equations, of course, there can be only a finite number of periodic solutions, each corresponding to a normal mode of the discretization matrix. This situation is analogous to the case of the advection equation $\rho_t + u\rho_x = 0$ on a periodic domain, for which any initial condition $\rho(x,0) = f(x)$ is periodic in time. Upon numerical discretization of this equation, the dispersion relation is altered, an arbitrary initial condition may be expanded in normal modes, and each of these evolves with a different phase speed, causing artificial dispersion. Only the (finite denumerable) normal modes themselves are periodic.

When forcing is present in (3.7)–(3.8), i.e. $\alpha(t) = 1 - \epsilon\cos 2\bar{\omega}t$, the buoyancy modes evolve independently according to the Mathieu equation

$$\frac{d^2}{dt^2}\tilde{b}_i = -(1 - \epsilon\cos 2\bar{\omega}t)\omega_i^2\tilde{b}_i.$$

The Mathieu equation supports resonance zones in parameter space for which the solution grows unbounded in magnitude as well as stable (non-resonant) zones for which the solution remains bounded for all time. The first and the most important instability region originates at the subharmonic frequency $\bar{\omega}$ of the driving frequency $2\bar{\omega}$, (see Arnold 1989).

3.3. *Dynamics of the Mathieu equation*

Write the scalar Mathieu equation in the general form

$$\frac{d^2}{dt^2}\beta + (a - 2q\cos(2t))\beta = 0. \tag{3.9}$$

According to the Floquet multiplier theorem, the Mathieu equation for fixed a and q admits a complex valued general solution of the form

$$\beta(t) = c_1 e^{\mu t} P(a, q, t) + c_2 e^{-\mu t} P(a, q, -t),$$

where $\mu \neq 0$ is a complex Floquet exponent and $P(a, q, t)$ is a complex valued, π-periodic, special function, i.e., $P(a, q, t + \pi) = P(a, q, t)$. If $\operatorname{Re}\mu = 0$, the solution $\beta(t)$ is bounded for all time. If $\operatorname{Re}\mu \neq 0$, the amplitude of the oscillations grows exponentially. For the degenerate case $\mu = 0$, the solutions are linearly dependent and the amplitude grows linearly in time.

To determine μ we note that taking initial conditions $\beta(0) = 1$, $\dot{\beta}(0) = 0$, one finds $c_1 = c_2 = (2P(a, q, 0))^{-1}$, hence the solution at time $t = \pi$ is

$$\beta(\pi) = \cosh\mu\pi. \tag{3.10}$$

Therefore μ can be estimated by solving (3.9) numerically on the interval $[0, \pi]$.

Our goal is to compute the two internal wave attractors presented in Section 2 by use of the parametric excitation mechanism described above. The values of θ and $\bar{\omega}/N_f$ are given in Figure 4. In our computations we will fix $\epsilon = 0.1$ and set $\bar{\omega} = \pi/2$. In Figure 5 we plot the real part of the Floquet exponent μ in the parameter domain $\bar{\omega}/N_f$ versus ϵ where the Floquet exponent is found from equation (3.10). To find the solution $\beta(\pi)$ of the Mathieu equation (3.9) with initial conditions $\beta(0) = 1$ and $\dot{\beta}(0) = 0$ we solve the Mathieu equation numerically using the Störmer-Verlet method (Hairer *et al.* 2006). In Figure 5(a) we see only one instability tongue but in Figure 5(b) we see two of them. This is due to the fact that we set the forcing frequency to $2\bar{\omega} = \pi$ that parametrically excites the subharmonic at frequency $\bar{\omega}$. Choosing $N_f = 100\pi/148$ in Figure 5(a), this implies that all of its super harmonics, $n\bar{\omega}$, $(n = 2, 3, \ldots)$, lie above the internal wave cut-off frequency, $n\bar{\omega} > N_f$. While for $N_f = 100\pi/68$ in Figure 5(b), its second harmonic is still below this cut-off. Consequently the range of the frequencies in the second example is greater than in the first one, and this explains the presence of two instability tongues in Figure 5(b). Since the forced internal wave equations (3.3)–(3.4) can be decomposed into the Mathieu type equations (3.7)–(3.8), the theory of Mathieu equations suggests that depending on the values of the Floquet exponent there will be resonant normal modes which will grow exponentially in time and there will be other modes which will stay bounded. The presence of resonant normal modes is dependent on the initial conditions. If a particular initial condition is such that its projection onto normal modes has no components within resonant zones of the Mathieu equation, then the solution of the forced linear internal wave equations (3.3)–(3.4) will stay bounded for all times. Hence the choice of initial conditions for computations is not arbitrary. The analysis in §4.1 of the system's response to different initial conditions in the unforced, undamped linear case suggests that the natural choice for finding $(1, 1)$ and $(1, 3)$ attractors would be initial conditions $\psi_{1,1}$ and $\psi_{1,3}$, respectively. This implies that there will be resonant normal modes.
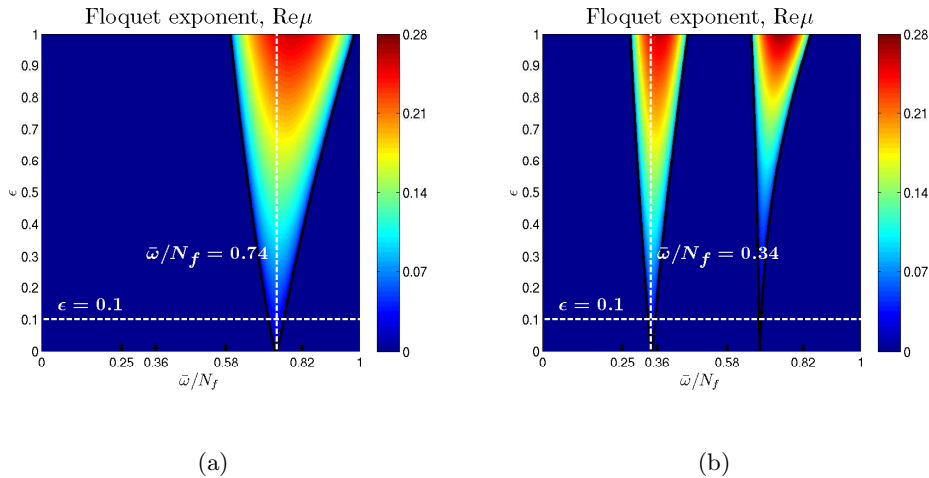
(a)   (b)

FIGURE 5. Instability tongues of the Mathieu equation, the real part of the Floquet exponent for the given values of $\bar{\omega}/N_f$ and ϵ. Left: one instability tongue in the computation of the $(1,1)$ attractor, $\bar{\omega}/N_f = 0.74$ and $\epsilon = 0.1$. Right: two instability tongues in the computation of the $(1,3)$ attractor, $\bar{\omega}/N_f = 0.34$ and $\epsilon = 0.1$.
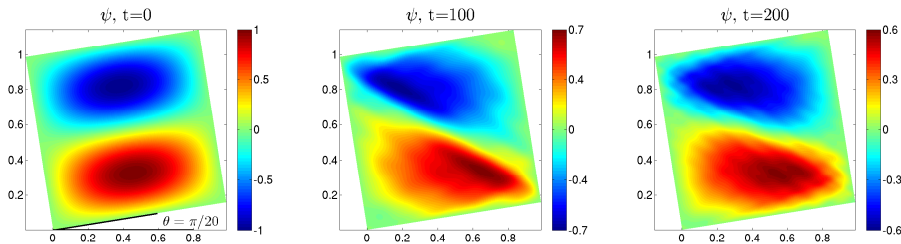

FIGURE 6. Evolution of the stream function in time from the initial condition $\psi_{1,2}$.

4. Numerical experiments

4.1. *Freely evolving flow*

Armed with the theory of internal gravity wave attractors in a tilted square from §2 and the structure preserving discretization of the Euler-Boussinesq equations in the stream function formulation from §3 we study the initial boundary value problem. Since we consider the inviscid equations, the system does not depend on spatial scales and time can be rescaled with respect to stratification frequency N_f to cast the system in dimensionless form. As we will see in the following, the response of the system will depend on tilt angle θ and on the choice of the initial conditions.

We study the response of the system with the Fourier mode initial conditions:

$$\psi_0(x,z) = \psi_{n,m}(x,z), \qquad b_0(x,z) \equiv 0, \qquad (n,m) = (1,1),(1,2),(1,3). \qquad (4.1)$$

These initial conditions correspond to low wavenumber smooth functions. When $\theta = 0$ the Fourier modes are eigenfunctions, as described in §3.1, and all three initial conditions result in single frequency standing wave solutions whose frequency is determined by the dispersion relation (2.12). When $\theta \neq 0$, i.e. the domain is tilted by the angle θ or the
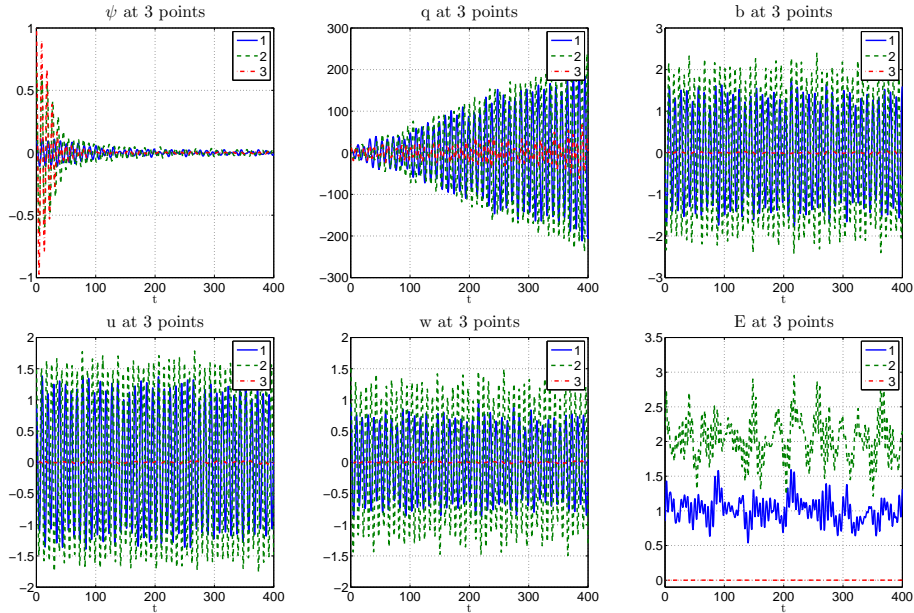
FIGURE 7. Time series of the stream function, vorticity, buoyancy, velocity u, velocity w and energy density function E at 3 points in space from computations with initial condition $\psi_{1,1}$ and $b = 0$.

direction of gravity is changed, the Fourier modes are no longer eigenfunctions, and we observe a different response from the system for initial conditions (4.1).

In all three numerical examples we use the same numerical parameters and parameter values. We compute to final time $T_{\text{end}} = 400$ with time step $\tau = 0.05$. The spatial mesh sizes in both space dimensions are equal, $\Delta x = \Delta z = 2 \times 10^{-3}$. We fix the stratification frequency $N_f = 1$ and choose $\theta = \pi/20$ for the rotation angle of the square. The Störmer-Verlet method (A 14)–(A 17) conserves energy in time up to fluctuations of amplitude $\mathcal{O}(\tau^2)$. For this choice of τ the relative error of the Hamiltonian function (3.6) remained smaller than 10^{-3} in all three numerical experiments. Computational results with initial conditions $\psi_{1,1}$ and $\psi_{1,3}$ are shown in Figure 2. Results with the initial condition $\psi_{1,2}$ are shown in Figure 6. In all three examples we plot the evolution of the stream function at three distinct times.

Complementary to the state variables we also look at the energy density function, i.e. the distribution of the energy in space. Hence we define the discrete energy density function at the cell centers, making use of the discrete velocities defined by (A 7),

$$E_{i+1/2,j+1/2} = \frac{1}{2}u_{i+1/2,j+1/2}^2 + \frac{1}{2}w_{i+1/2,j+1/2}^2 + \frac{1}{2N_f^2}b_{i+1/2,j+1/2}^2. \qquad (4.2)$$

In the numerical example with initial condition $\psi_{1,1}$ we observe that energy that is initially concentrated at the low wavenumber is transported to large wave numbers. Evidently, in Figure 2 the whole family of $(1, 1)$ attractors is observable. The evolution from initial condition $\psi_{1,3}$ is similar, but in this case the family of $(1, 3)$ wave attractors is obtained, see Figure 2. On the other hand, with initial condition $\psi_{1,2}$ the solution appears to consist mainly of a strong periodic component, plus small scale fluctuations.

Despite the fact that the energy functional (2.9) is conserved along the solution of the continuous system (2.5)–(2.8) and the discrete energy function (3.6) is conserved

up to second order in time† along the solution of the discrete system (A 14)–(A 17), the amplitude of the stream function decays. That can be seen by comparing the color bars in Figures 2 and 6. For total energy to remain constant, there should either be a net exchange of kinetic into potential energy, or the amplitude of vorticity should grow commensurate to the loss in stream function. To confirm this we study the time series of the state variables: stream function, vorticity, buoyancy, velocities (A 7) and the energy density function (4.2), at three arbitrarily chosen points in space. These three points are shown in the top left plot of Figure 2. In Figure 7 we plot numerical time series data at these three points for the initial condition $\psi_{1,1}$. From Figure 7 we see that for energy to stay bounded when the amplitude of the stream function decays the amplitude of the vorticity grows and buoyancy, energy density function and the components of the velocity field stay bounded. This is reminiscent of the familiar cascade of vorticity to large wave numbers in 2D fluids, but note that the nonlinear advection terms are neglected in this model, so the observed effect is really due to dispersion among the normal modes. In fact, the unforced problem is quasiperiodic, so all such trends must eventually reverse.

The presence of only a single family of wave attractors in the time evolution of the initial conditions $\psi_{1,1}$ and $\psi_{1,3}$ suggests the excitation of only those frequencies associated to the respective class of $(1,1)$ and $(1,3)$ wave attractors, respectively. Similarly, the nearly periodic evolution from the $\psi_{1,2}$ Fourier mode suggests the dominance of the periodic $(1,2)$ solution.

To understand this, we project the Fourier modes onto the normal modes of the tilted system. We expand the initial conditions (4.1) in the normal modes of the semi-discretization (3.3)–(3.4) for $\theta = \pi/20$ and $N_f = 1$. We plot the scaled discrete energy values $H_i/\max\{H_i\}$ with respect to the frequencies of the discrete system in Figures 8(a), 8(b) and 8(c). In each of these Figures we plot a dashed blue line to indicate the standing wave solution frequency for $\theta = 0$. Figure 8(d) contains a diagram of the limit behavior of frequencies for a tilt angle $\theta = \pi/20$. Black horizontal line segments indicate the ranges of frequencies for limit cycle attractors having a period less than eighteen for $\theta = \pi/20$. For $\theta = \pi/20$ there exist only six periodic solutions of type $(2n,1)$ and $(1,2m)$ indicated with the dashed blue lines. Comparing Figures 8(d) and 8(a) we see that the $(1,1)$-Fourier mode projects almost entirely onto the range of $(1,1)$-attractors. Since there is no energy transfer between normal modes the solution of the semi discrete system with initial conditions $\psi_{1,1}$ at any time is a linear combination of the normal modes with frequencies in the range of the $(1,1)$ attractors. Similarly, most of the energy in the $(1,3)$-Fourier mode projects into the range of $(1,3)$ attractors. In contrast, Figure 8(b) illustrates that the $(1,2)$-Fourier mode is concentrated at one discrete frequency, which is very near that of the $(1,2)$ periodic solution, explaining the nearly periodic behavior of this solution.

For future reference, Figure 9 shows the most energetic normal modes with frequencies within the $(1,1)$ and $(1,3)$ attractor ranges, and the distinct normal mode with $(1,2)$ periodic solution frequency.

4.2. *Computation of wave attractors*

In Section 2 we described how to compute monochromatic wave solutions in a tilted square. We illustrated this with two examples of internal gravity wave attractors, see

† Backward error analysis of symplectic numerical integrators (Hairer *et al.* 2006; Leimkuhler & Reich 2004) shows the existence of a perturbed Hamiltonian of the form $H + \mathcal{O}(\tau^2)$ which is exactly conserved. For our problem, this implies the total energy will be conserved up to bounded fluctuations with amplitude $\mathcal{O}(\tau^2)$.
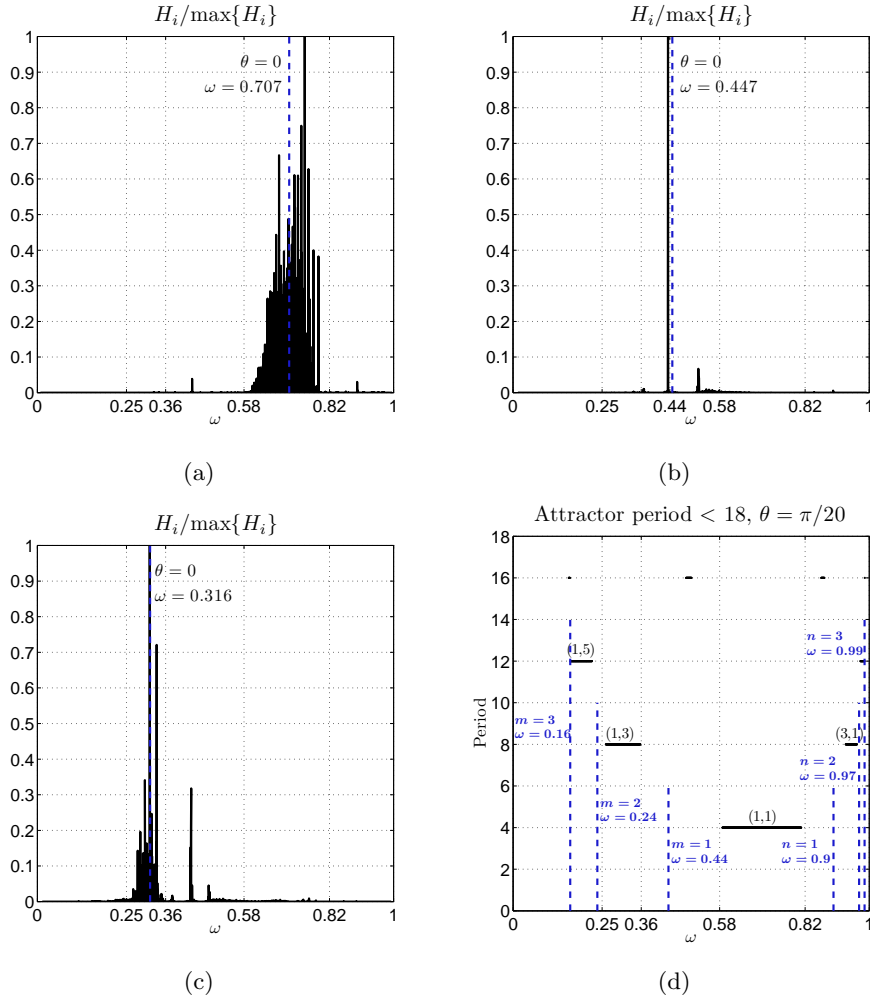
FIGURE 8. Scaled energy values with respect to the frequencies of the semi discrete system (3.3)–(3.4) for the initial conditions $\psi_{1,1}$, $\psi_{1,2}$ and $\psi_{1,3}$, top left, top right and bottom left, respectively. Bottom right: section plot of the attractor period Figure 3(b) for the fixed angle $\theta = \pi/20$. Bars and dashed lines are discussed in the text.

Figures 4(a) and 4(b). In this section we compute internal wave attractors as an initial value problem with parametric excitation, so-called parametric resonance solutions.

We solve (3.3)–(3.4) with the Störmer-Verlet method. Since we generate instability in the system by parametric excitation, the amplitude of the solution grows in time, and energy is no longer conserved. We set forcing frequency to $2\bar{\omega} = \pi$ so that we have integer wave period $T = 4$. The other two parameters θ and N_f are determined by the type of limit behavior we want to simulate. We compute a $(1, 1)$ attractor with parameter values $\bar{\omega}/N_f = 0.74$ and $\theta = 7\pi/72$, and a $(1, 3)$ attractor with parameter values $\bar{\omega}/N_f = 0.34$ and $\theta = \pi/18$.

Numerical parameters are fixed for both experiments: the forcing amplitude $\epsilon = 0.1$, time step $\tau = 0.05$ and grid step sizes $\Delta x = \Delta z = 2 \times 10^{-3}$. Initial conditions are chosen to be the Fourier modes $\psi_{1,1}$ and $\psi_{1,3}$ in the computation of the $(1, 1)$ and $(1, 3)$ attractors, respectively. We force the system for 50 wave periods and plot the stream
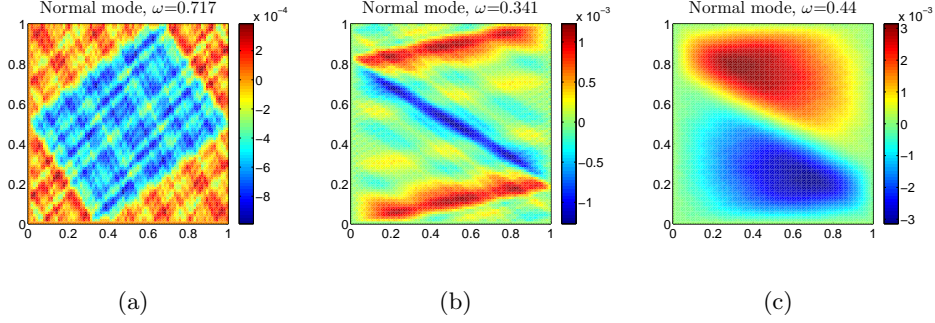
FIGURE 9. Normal modes of the stream function, $N_f = 1$ and $\theta = \pi/20$. Left: associated to the frequency of $(1,1)$ attractor. Middle: associated to the frequency of $(1,3)$ attractor. Right: associated to the frequency of $(1,2)$ periodic solution.
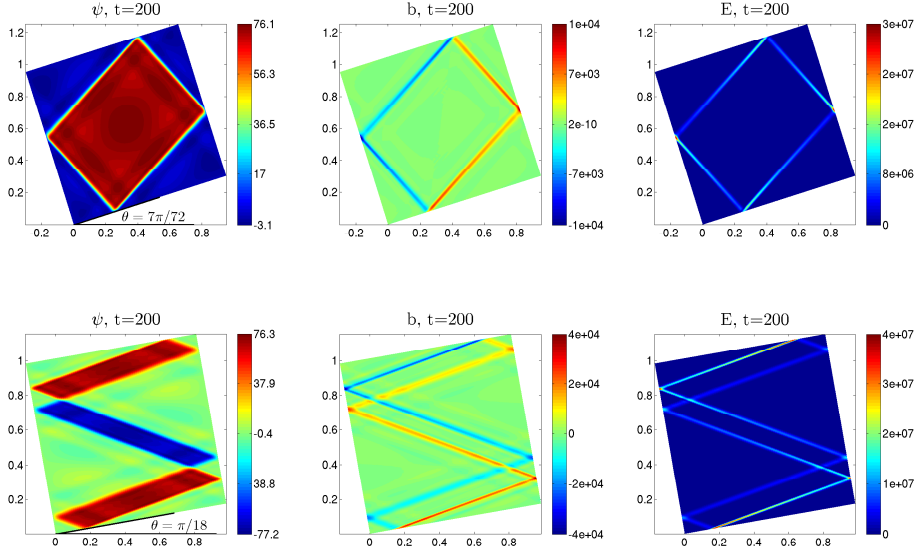

FIGURE 10. Computation of $(1,1)$ (top) and $(1,3)$ attractor (bottom). The stream function (left), buoyancy (middle) and energy density (right) after 50 wave periods. Initial conditions are the same as in Figure 2 at time $t = 0$.

function, buoyancy and the discrete energy density function (4.2) at the final time in Figure 10.

Figure 10 (top) displays the results for the $(1,1)$ limit cycle attractor. The energy is focused on the attractor, which reflects from each side of the square once. We observe a standing wave solution with growing amplitude and a 'plateau' type of attractor with piecewise constant stream function. After about 10 wave periods, i.e. at time $t = 40$, the wave motion becomes localized along the straight lines of the attractor. The same 'plateau' type of attractors where observed in laboratory experiments (Hazewinkel *et al.* 2008). Since all sides of the tilted square are inclined, in the case of a simple $(1,1)$ attractor, internal waves become focused at all boundaries, because the energy is transported

in a counter-clockwise orientation around the attractor, as is indicated in the plots of the energy density function†, see the right top plot of Figure 10.

In Figure 10 (bottom) we consider an example of a $(1, 3)$ attractor. It has one intersection point with the upper and lower boundaries of the square, and three intersection points each on the left and right sides of the square. Similarly to the case of the $(1, 1)$ attractor, we observe a standing wave solution that grows in amplitude, and the wave energy is localized along the straight lines of an attractor. The form of the attractor is again of 'plateau' type. Internal waves become highly focused upon reflection from the upper and lower boundaries of the square and gradually defocus in the rest of the domain, see the right bottom plot of Figure 10.

By the arguments of §4.1, the choice of the initial conditions $\psi_{1,1}$ and $\psi_{1,3}$ ensures that there will be energy in the normal modes corresponding to $(1, 1)$ and $(1, 3)$ attractors, a subset of which will grow in amplitude due to resonance of the underlying Mathieu equations. Those modes with frequencies outside the instability tongue of the Mathieu equations remain bounded for all times and eventually become negligible compared to the unstable modes. Since we do not have external damping (like in the experiment discussed in Maas *et al.* (1997); Lam & Maas (2008)), they also do not dissipate. Evolution of the stable modes is primarily significant only during the early part of the simulation, before the wave attractor dominates.

Experiments with smaller values of ϵ result in a decrease in the width of the attractors. Figure 5 suggests that early on in the computation all the normal modes with frequencies in the resonant zone contribute to the dynamics. But since those modes for which the real part of the Floquet exponent is greater grow much faster in time, these become more prominently visible than others. Because of this the width of an attractor becomes narrower and narrower in time. While the white dashed lines in Figure 5 indicated with $\bar{\omega}/N_f = 0.74$ and $\bar{\omega}/N_f = 0.34$ almost divide the Arnold tongues in half, if one wishes to simulate a particular attractor geometry, it is advisable to use small values of ϵ such that among all resonant normal modes exactly the one associated to the frequency of the desired attractor has the Floquet multiplier with largest real part.

Since there is no exchange of energy between normal modes, the precise structure observed at large times will depend both on the associated Floquet multipliers, and on the initial distribution of energy among the resonant frequencies. In other words, the initial condition is relevant to what is observed in Figure 10. In the presence of viscosity, the various normal modes do not evolve independently, and the asymptotic solution is independent of the initial condition (Ogilvie 2005).

The primary solutions observed in Figure 10 are of plateau type. These solutions are composite, consisting of a linear combination of the resonant modes. Typical normal modes are nonsmooth, for example, as shown in Figure 9. Close inspection of the solutions in Figure 10 reveal that there are secondary oscillations added to the plateau solution. To better observe these, we subtract the plateau solution using the following formula:

$$\delta\psi_{i,j} = \mathrm{trunc}\left(\frac{\psi_{i,j} - \min\{\boldsymbol{\psi}\}}{\max\{\boldsymbol{\psi} - \min\{\boldsymbol{\psi}\}\}}k\right), \qquad \mathrm{trunc}(f) = f - \lfloor f \rfloor,$$

where $\lfloor f \rfloor$ indicates the largest integer less than f. The idea of the formula is to rescale the stream function, such that the oscillations about the plateau solution have an amplitude that is less than unity, and then subtract the integer part of the solution everywhere. This is achieved for the empirically chosen value $k = 12$. We plot the secondary wave solution

---

† Due to focusing, the energy density increases *after* reflection. Hence, the direction of energy propagation on the attractor can be deduced from the energy density plots.
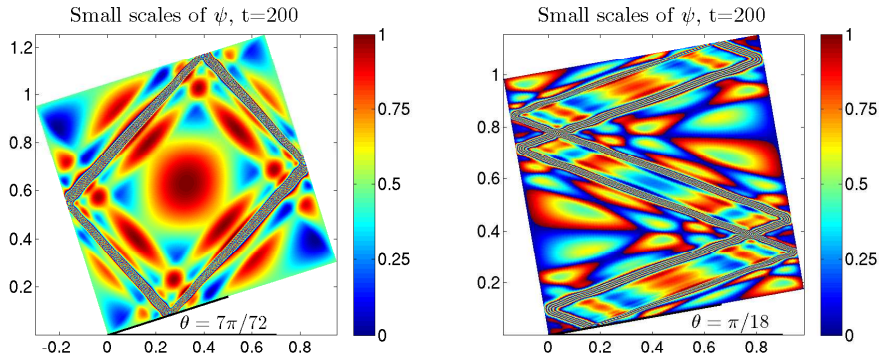
FIGURE 11. Small scales in the solution after 50 wave periods. Left: $(1,1)$ attractor. Right: $(1,3)$ attractor.

in Figure 11 for the stream function at final time $t = 200$. Note the symmetry of the solution and a passing resemblance to Figure 4. The secondary solutions are also robust with respect to spatial resolution and time step τ. The shape of the secondary solution and its robustness with respect to numerical parameters and perturbation amplitude ε suggests that the attractor shape is not truly piecewise constant, but has higher order secondary waveforms.

5. Conclusions

In this paper we have considered the simplest time dependent configuration in which internal wave attractors can be generated in stratified fluids: linearized, inviscid flow with parametric forcing. We constructed a symmetric, energy conserving finite difference method. For the case of a tilted square geometry we simulated both the free evolution (unforced) wave evolution from Fourier mode initial conditions, and the parametrically forced evolution towards a wave attractor. This simple configuration, as well as the symmetries of the discretization, permit a complete normal mode analysis of the initial value problem in the discrete case. Based on this analysis we can conclude that the finite dimensional approximation has a complete basis of normal modes that is invariant in time, meaning the initial value problem can be fully decoupled into scalar harmonic oscillators, each of which preserves its initial energy. Therefore, the numerical solution is quasiperiodic, although the Poincaré recurrence time (the time over which a discrete, energy conserving system recovers its initial state) may be quite large. The same analysis can be carried out for the parametrically forced case, showing that the forced system of ODEs can be completely decoupled into Mathieu equations. For a generic initial condition, and depending on the frequency and magnitude of forcing, a range of normal mode frequencies will lie in an Arnold tongue of instability, and the corresponding modes will grow in time, eventually dominating the solution and forming a wave attractor. The shape of the stream function is to first order a plateau, or piecewise constant function, but there are secondary solutions that are robust with respect to discretization and forcing parameters.

We remark that for a given forcing, it is possible to choose judiciously an initial condition whose projection onto the amplified frequencies of the Mathieu equation is zero. In this case, a wave attractor will never be generated. However, this no longer holds if

nonlinear advection is taken into account, due to nonlinear coupling. In fact, even for the linearized model, if viscosity is included there is no global decomposition into scalar dynamics, since the normal mode decomposition becomes time dependent.

Appendix A. Hamiltonian numerical discretization

The Euler equations for an ideal fluid have a well-known Hamiltonian structure (Arnold 1989; Morrison 1998) that strongly constrains the dynamics. When constructing approximate models such as the Euler-Boussinesq equations (2.1)–(2.4), it is usually advised to preserve such structure (Salmon 1998). As shown in Holm *et al.* (2002), the nonlinear Euler-Boussinesq equations inherit the noncanonical Hamiltonian structure from the ideal fluid Poisson bracket. Here we verify that the linearization leading to (2.5)–(2.8) also preserves a linear Hamiltonian structure. A system of PDEs on a function space $\boldsymbol{F}^d$ equipped with an inner product $(\cdot,\cdot) : \boldsymbol{F}^d \times \boldsymbol{F}^d \to \mathbb{R}$ is said to constitute a Hamiltonian system (Olver 1986) in the variables $\boldsymbol{f}(x,t) = (f_1(x,t), \ldots, f_d(x,t))^T \in \boldsymbol{F}^d$ if there exists a functional $\mathcal{H}(\boldsymbol{f}) : \boldsymbol{F}^d \to \mathbb{R}$ and a constant, $d \times d$ matrix differential operator (structure matrix) $\mathcal{J} : \boldsymbol{F}^d \to \boldsymbol{F}^d$, that is skew-symmetric with respect to $(\cdot,\cdot)$, such that the PDE can be expressed as

$$\partial_t \boldsymbol{f} = \mathcal{J} \frac{\delta \mathcal{H}}{\delta \boldsymbol{f}}, \tag{A 1}$$

where the variational derivative $\delta\mathcal{H}/\delta\boldsymbol{f}$ is defined by

$$\left(\frac{\delta\mathcal{H}}{\delta\boldsymbol{f}}, \boldsymbol{g} \right) = \lim_{\varepsilon \to 0} \frac{1}{\varepsilon} \left[\mathcal{H}(\boldsymbol{f} + \varepsilon\boldsymbol{g}) - \mathcal{H}(\boldsymbol{f}) \right], \quad \forall \boldsymbol{g} \in \boldsymbol{F}^d.$$

One consequence of Hamiltonian structure is the conservation of the Hamiltonian along solutions of (A 1), which follows from:

$$\frac{d\mathcal{H}}{dt} = \left(\frac{\delta\mathcal{H}}{\delta\boldsymbol{f}}, \partial_t \boldsymbol{f} \right) = \left(\frac{\delta\mathcal{H}}{\delta\boldsymbol{f}}, \mathcal{J} \frac{\delta\mathcal{H}}{\delta\boldsymbol{f}} \right) = 0,$$

by the skew-symmetry condition on $\mathcal{J}$.

We show:

PROPOSITION 1. *For any value of θ the linearized Euler-Boussinesq equations in the stream function formulation (2.5)–(2.8) can be written as a noncanonical Hamiltonian system (A 1) in the L^2 inner product with $\boldsymbol{f} = (q,b)$, structure matrix*

$$\mathcal{J} = -N_f^2 \cos\theta \begin{bmatrix} 0 & \partial_x \\ \partial_x & 0 \end{bmatrix} + N_f^2 \sin\theta \begin{bmatrix} 0 & \partial_z \\ \partial_z & 0 \end{bmatrix} \tag{A 2}$$

and Hamiltonian

$$\mathcal{H} = \frac{1}{2} \int_D \nabla\psi \cdot \nabla\psi + \frac{1}{N_f^2} b^2 \, d\boldsymbol{x}. \tag{A 3}$$

Proof. The first variations of the Hamiltonian functional (A 3) with respect to q and b are

$$\delta\mathcal{H} = \int_D \nabla\psi \cdot \nabla\delta\psi + \frac{1}{N_f^2} b\delta b \, d\boldsymbol{x} = \int_D -\psi\Delta\delta\psi + \frac{1}{N_f^2} b\delta b \, d\boldsymbol{x} = \int_D \psi\delta q + \frac{1}{N_f^2} b\delta b \, d\boldsymbol{x},$$

where the boundary condition (2.8) has been used to carry out the integration by parts.

It follows that the variational derivatives of the Hamiltonian (A 3) with respect to the vorticity q and the buoyancy b are

$$\frac{\delta \mathcal{H}}{\delta q} = \psi, \qquad \frac{\delta \mathcal{H}}{\delta b} = \frac{1}{N_f^2} b. \qquad (A\,4)$$

Substituting (A 4) and (A 2) into (A 1) we get that

$$\mathcal{J} \frac{\delta \mathcal{H}}{\delta \boldsymbol{f}} = \mathcal{J} \begin{pmatrix} \frac{\delta \mathcal{H}}{\delta q} \\ \frac{\delta \mathcal{H}}{\delta b} \end{pmatrix} = \begin{pmatrix} -\partial_x b \cos \theta + \partial_z b \sin \theta \\ -N_f^2 (\partial_x \psi \cos \theta + \partial_z \psi \sin \theta) \end{pmatrix} = \begin{pmatrix} \partial_t q \\ \partial_t b \end{pmatrix} = \partial_t \boldsymbol{f}$$

which agree with (2.5)–(2.8) $\square$

It follows that the Hamiltonian functional (A 3) is conserved along the solution of the equation system (2.5)-(2.8).

A.1. *Finite difference matrices*

In this section we describe a numerical discretization for the Euler-Boussinesq equations that preserves a discrete analogue of the Hamiltonian structure in the inviscid, unforced limit. In particular the spatially discrete system of ODEs has a first integral approximating the energy. The scheme also preserves the symmetries of the continuous differential operators. Our approach is to discretize the Hamiltonian and structure operator $\mathcal{J}$ separately, while enforcing the skew-symmetry of $\mathcal{J}$, (see McLachlan 1995). Although this approach leads to a rather standard staggered central difference scheme here, it can be used to construct a Hamiltonian discretization on more general domains and nonuniform grids, which will be important for studying internal waves in ocean basins.

Consider the unit square domain $D = [0,1]^2$ divided into $N_x \times N_z$ uniform rectangular cells. Subscripted indices shall indicate grid nodes $\boldsymbol{x}_{i,j} = (i\Delta x, j\Delta z)$, where $\Delta x = 1/N_x$ and $\Delta z = 1/N_z$ are the grid sizes in x and z direction, respectively. We shall construct a Hamiltonian structure-preserving staggered finite difference scheme. To this end let us denote by $\mathbf{C} = \mathbb{R}^{N_x \times N_z}$ the space of cell-centered grid functions and by $\mathbf{V} = \mathbb{R}^{(N_x-1) \times (N_z-1)}$ the space of grid functions defined at cell vertices, where in the latter case, we only include inner vertices, since the boundary vertices are either known, or not needed in the discretization.

The discrete stream function $\psi_{i,j}$ and vorticity $q_{i,j}$ are defined at cell vertices and the buoyancy $b_{i+1/2,j+1/2}$ at cell centers. The discrete analogue of the boundary condition on the stream function (2.8) is

$$\psi_{0,j} = \psi_{N_x,j} = 0, \quad \forall j, \qquad \psi_{i,0} = \psi_{i,N_z} = 0, \quad \forall i. \qquad (A\,5)$$

We define column vectors $\boldsymbol{q}, \boldsymbol{\psi} \in \mathbf{V}$ consisting only of the interior grid point values of $q_{i,j}$ and $\psi_{i,j}$. The buoyancy column vector $\boldsymbol{b} \in \mathbf{C}$ consists of all the values of $b_{i+1/2,j+1/2}$ defined at cell centers.

We also define discrete inner products on $\mathbf{C}$ and $\mathbf{V}$:

$$\langle \boldsymbol{a}, \boldsymbol{b} \rangle_{\mathbf{C}} = \sum_{i,j=0}^{N_x-1,N_z-1} a_{i+1/2,j+1/2} b_{i+1/2,j+1/2} \, \Delta x \, \Delta z, \quad \boldsymbol{a}, \boldsymbol{b} \in \mathbf{C},$$

$$\langle \boldsymbol{q}, \boldsymbol{r} \rangle_{\mathbf{V}} = \sum_{i,j=1}^{N_x-1,N_z-1} q_{i,j} r_{i,j} \, \Delta x \, \Delta z. \quad \boldsymbol{q}, \boldsymbol{r} \in \mathbf{V}.$$

For the inner product on $\mathbf{V}$ we assume zero boundary data for at least one of its arguments.

Taking into account the discrete boundary conditions (A 5), the following matrices implement the central finite difference approximations to the first derivatives on cell edges:

$$(D_x\boldsymbol{\psi})_{i+1/2,j} = \frac{\psi_{i+1,j} - \psi_{i,j}}{\Delta x}, \qquad (D_z\boldsymbol{\psi})_{i,j+1/2} = \frac{\psi_{i,j+1} - \psi_{i,j}}{\Delta z},$$

where $D_x \in \mathbb{R}^{N_x(N_z-1)\times(N_x-1)(N_z-1)}$ and $D_z \in \mathbb{R}^{N_z(N_x-1)\times(N_x-1)(N_z-1)}$. The dual operators $-D_x^T$ and $-D_z^T$ represent central finite difference approximations to the first derivatives on cell vertices from cell edges.

Additionally we define the averaged operator matrices $M_x \in \mathbb{R}^{N_z(N_x-1)\times N_x N_z}$ and $M_z \in \mathbb{R}^{N_x(N_z-1)\times N_x N_z}$ from cell centers to cell edges such that

$$(M_x\boldsymbol{b})_{i,j+1/2} = \frac{b_{i+1/2,j+1/2} + b_{i-1/2,j+1/2}}{2}, \quad (M_z\boldsymbol{b})_{i+1/2,j} = \frac{b_{i+1/2,j+1/2} + b_{i+1/2,j-1/2}}{2},$$

where their transposes are averaged operator matrices from the cell edges to the cell centers.

The matrices above can be composed in various ways to construct approximate derivative operators from $\mathbf{V}$ to $\mathbf{C}$ and vice versa.

$$M_z^T D_x : \mathbf{V} \to \mathbf{C}, \quad M_x^T D_z : \mathbf{V} \to \mathbf{C}, \quad -M_z D_x^T : \mathbf{C} \to \mathbf{V}, \quad -M_z^T D_x : \mathbf{C} \to \mathbf{V}.$$

The discrete Laplacian operator $L : \mathbf{V} \to \mathbf{V}$, defined as

$$L = -(D_x^T D_x + D_z^T D_z) \in \mathbb{R}^{(N_x-1)(N_z-1)\times(N_x-1)(N_z-1)}, \tag{A 6}$$

is the standard symmetric, negative definite, five point central difference stencil, i.e.,

$$(L\boldsymbol{\psi})_{i,j} = \frac{\psi_{i+1,j} - 2\psi_{i,j} + \psi_{i-1,j}}{\Delta x^2} + \frac{\psi_{i,j+1} - 2\psi_{i,j} + \psi_{i,j-1}}{\Delta z^2},$$

where the boundary terms are modified to satisfy (A 5). We define the discrete vorticity field by $\boldsymbol{q} = -L\boldsymbol{\psi}$.

For diagnostic purposes we also define the discrete velocity components at cell centers:

$$\boldsymbol{u} = -M_x^T D_z \boldsymbol{\psi}, \qquad \boldsymbol{v} = M_z^T D_x \boldsymbol{\psi}. \tag{A 7}$$

A.2. *Hamiltonian semi-discretization*

To construct a Hamiltonian semi-discretization with structure analogous to (A 2), we define a quadrature for H and a skew-symmetric structure that approximates $\mathcal{J}$.

In terms of inner products on $\mathbf{C}$ and $\mathbf{V}$, the discrete Hamiltonian is defined by

$$H(\boldsymbol{q}, \boldsymbol{b}) = \frac{1}{2}\left(-\langle\boldsymbol{\psi}, \boldsymbol{q}\rangle_\mathbf{V} + \frac{1}{N_f^2}\langle\boldsymbol{b}, \boldsymbol{b}\rangle_\mathbf{C}\right) = \frac{1}{2}\left(-\langle\boldsymbol{q}, L^{-1}\boldsymbol{q}\rangle_\mathbf{V} + \frac{1}{N_f^2}\langle\boldsymbol{b}, \boldsymbol{b}\rangle_\mathbf{C}\right). \tag{A 8}$$

The variational derivatives of H are defined in the weak sense in these inner products by

$$\langle\frac{\delta H}{\delta\boldsymbol{q}}, \boldsymbol{r}\rangle_\mathbf{V} = \lim_{\varepsilon\to 0}\frac{1}{\varepsilon}\left(H(\boldsymbol{q}+\varepsilon\boldsymbol{r}, \boldsymbol{b}) - H(\boldsymbol{q}, \boldsymbol{b})\right) = \langle\boldsymbol{\psi}, \boldsymbol{r}\rangle_\mathbf{V}, \qquad \forall\boldsymbol{r}\in\mathbf{V},$$

$$\langle\frac{\delta H}{\delta\boldsymbol{b}}, \boldsymbol{a}\rangle_\mathbf{C} = \lim_{\varepsilon\to 0}\frac{1}{\varepsilon}\left(H(\boldsymbol{q}, \boldsymbol{b}+\varepsilon\boldsymbol{a}) - H(\boldsymbol{q}, \boldsymbol{b})\right) = \langle\frac{1}{N_f^2}\boldsymbol{b}, \boldsymbol{a}\rangle_\mathbf{C}, \qquad \forall\boldsymbol{a}\in\mathbf{C},$$

i.e.,

$$\frac{\delta H}{\delta\boldsymbol{q}} = \boldsymbol{\psi}, \qquad \frac{\delta H}{\delta\boldsymbol{b}} = \frac{1}{N_f^2}\boldsymbol{b}.$$

Next, we define a composite space $\boldsymbol{G} = \mathbf{V} \times \mathbf{C}$. A vector $\boldsymbol{g} \in \boldsymbol{G}$ takes the form

$$\boldsymbol{g} = \begin{pmatrix} \boldsymbol{g_\mathbf{V}} \\ \boldsymbol{g_\mathbf{C}} \end{pmatrix},$$

where $\boldsymbol{g_\mathbf{V}} \in \mathbf{V}$ and $\boldsymbol{g_\mathbf{C}} \in \mathbf{C}$. We also define a joint inner product on $\boldsymbol{G}$:

$$\langle\!\langle \boldsymbol{g}, \boldsymbol{h} \rangle\!\rangle = \langle \boldsymbol{g_\mathbf{V}}, \boldsymbol{h_\mathbf{V}} \rangle_\mathbf{V} + \langle \boldsymbol{g_\mathbf{C}}, \boldsymbol{h_\mathbf{C}} \rangle_\mathbf{C},$$

and the variational derivative

$$\frac{\delta H}{\delta \boldsymbol{g}} = \begin{pmatrix} \frac{\delta H}{\delta \boldsymbol{g_\mathbf{V}}} \\ \frac{\delta H}{\delta \boldsymbol{g_\mathbf{C}}} \end{pmatrix}.$$

We approximate the structure operator (A 2) using our finite difference matrices:

$$J = -N_f^2 \cos\theta \begin{bmatrix} 0 & -D_x^T M_z \\ M_z^T D_x & 0 \end{bmatrix} + N_f^2 \sin\theta \begin{bmatrix} 0 & -D_z^T M_x \\ M_x^T D_z & 0 \end{bmatrix}. \qquad (A\,9)$$

Note that J is skew-symmetric with respect to $\langle\!\langle \cdot, \cdot \rangle\!\rangle$.

Choosing $\boldsymbol{g} = (\boldsymbol{q}, \boldsymbol{b})$, the Hamiltonian semi-discretization of the Euler-Boussinesq equations can now be defined by

$$\frac{d\boldsymbol{g}}{dt} = J \frac{\delta H}{\delta \boldsymbol{g}}. \qquad (A\,10)$$

or, in terms of $\boldsymbol{q}$, $\boldsymbol{b}$ and $\boldsymbol{\psi}$,

$$\frac{d\boldsymbol{q}}{dt} = D_x^T M_z \boldsymbol{b} \cos\theta - D_z^T M_x \boldsymbol{b} \sin\theta, \qquad (A\,11)$$

$$\frac{d\boldsymbol{b}}{dt} = -N_f^2 (M_z^T D_x \boldsymbol{\psi} \cos\theta - M_x^T D_z \boldsymbol{\psi} \sin\theta), \qquad (A\,12)$$

$$\boldsymbol{q} = -L\boldsymbol{\psi}. \qquad (A\,13)$$

By construction the discrete total energy H is a first integral of the semi-discretization. Additionally, this system of ODEs is reversible and symplectic.

A.3. *Time integration*

We have shown that semi-discrete Euler-Boussinesq equations (A 11)–(A 13) constitute a time-revesible Hamiltonian system. We solve the Hamiltonian system in time with the symmetric and symplectic Störmer-Verlet method (Hairer *et al.* 2006; Leimkuhler & Reich 2004):

$$\boldsymbol{q}^{n+1/2} = \boldsymbol{q}^n + \frac{\tau}{2}(D_x^T M_z \boldsymbol{b}^n \cos\theta - D_z^T M_x \boldsymbol{b}^n \sin\theta), \qquad (A\,14)$$

$$\boldsymbol{\psi}^{n+1/2} = -L^{-1} \boldsymbol{q}^{n+1/2}, \qquad (A\,15)$$

$$\boldsymbol{b}^{n+1} = \boldsymbol{b}^n - \tau N_f^2 (M_z^T D_x \boldsymbol{\psi}^{n+1/2} \cos\theta - M_x^T D_z \boldsymbol{\psi}^{n+1/2} \sin\theta), \qquad (A\,16)$$

$$\boldsymbol{q}^{n+1} = \boldsymbol{q}^{n+1/2} + \frac{\tau}{2}(D_x^T M_z \boldsymbol{b}^{n+1} \cos\theta - D_z^T M_x \boldsymbol{b}^{n+1} \sin\theta), \qquad (A\,17)$$

such that the Hamiltonian function (A 8) will be conserved in time up to small fluctuations of second order amplitude. The method requires the solution of the Poisson equation once per time step, but is otherwise explicit. We solve the Poisson equation efficiently using a fast Poisson solver. The overall method is second order in space and time. Sparse discretization in space combined with a fast Poisson solver allows us to compute efficiently at high spatial resolution.

Appendix B. Normal mode decomposition of discretized linear internal waves

We next consider the discrete model (3.3)–(3.4) with parametric forcing, written in terms of the stream function $\boldsymbol{\psi} \in \mathbb{R}^M$ and buoyancy $\boldsymbol{b} \in \mathbb{R}^N$:

$$\begin{bmatrix} -L & 0 \\ 0 & \frac{1}{N_f^2} I_N \end{bmatrix} \frac{d}{dt} \begin{pmatrix} \boldsymbol{\psi} \\ \boldsymbol{b} \end{pmatrix} = \begin{bmatrix} 0 & \alpha(t)K \\ -K^T & 0 \end{bmatrix} \begin{pmatrix} \boldsymbol{\psi} \\ \boldsymbol{b} \end{pmatrix}, \tag{B1}$$

where $N = N_x N_z$, $M = (N_x - 1)(N_z - 1)$, $L \in \mathbb{R}^{M \times M}$ is the discrete approximation of the Laplacian (A6), $K \in \mathbb{R}^{M \times N}$ is a finite difference matrix

$$K = D_x^T M_z \cos\theta - D_z^T M_x \sin\theta$$

and I_N denotes the identity matrix on $\mathbb{R}^N$. The matrix L is symmetric and negative definite, and hence possesses an orthogonal basis of eigenvectors, and we can write $-L = Q D_L Q^T$, where $Q^T Q = Q Q^T = I_M$, $Q \in \mathbb{R}^{M \times M}$ and $D_L \in \mathbb{R}^{M \times M}$ is a diagonal matrix with positive entries. In matrix form we write

$$\begin{bmatrix} Q D_L Q^T & 0 \\ 0 & \frac{1}{N_f^2} I_N \end{bmatrix} \frac{d}{dt} \begin{pmatrix} \boldsymbol{\psi} \\ \boldsymbol{b} \end{pmatrix} = \begin{bmatrix} 0 & \alpha(t)K \\ -K^T & 0 \end{bmatrix} \begin{pmatrix} \boldsymbol{\psi} \\ \boldsymbol{b} \end{pmatrix}.$$

We transform as follows:

$$\begin{bmatrix} Q D_L^{1/2} & 0 \\ 0 & \frac{1}{N_f} I_N \end{bmatrix} \begin{bmatrix} D_L^{1/2} Q^T & 0 \\ 0 & \frac{1}{N_f} I_N \end{bmatrix} \frac{d}{dt} \begin{pmatrix} \boldsymbol{\psi} \\ \boldsymbol{b} \end{pmatrix}$$
$$= \begin{bmatrix} 0 & \alpha(t)K \\ -K^T & 0 \end{bmatrix} \begin{bmatrix} Q D_L^{-1/2} & 0 \\ 0 & N_f I_N \end{bmatrix} \begin{bmatrix} D_L^{1/2} Q^T & 0 \\ 0 & \frac{1}{N_f} I_N \end{bmatrix} \begin{pmatrix} \boldsymbol{\psi} \\ \boldsymbol{b} \end{pmatrix}$$

or, defining $\hat{\boldsymbol{\psi}} = D_L^{1/2} Q^T \boldsymbol{\psi}$ and $\hat{\boldsymbol{b}} = \frac{1}{N_f} \boldsymbol{b}$,

$$\frac{d}{dt} \begin{pmatrix} \hat{\boldsymbol{\psi}} \\ \hat{\boldsymbol{b}} \end{pmatrix} = N_f \begin{bmatrix} 0 & \alpha(t) D_L^{-1/2} Q^T K \\ -K^T Q D_L^{-1/2} & 0 \end{bmatrix} \begin{pmatrix} \hat{\boldsymbol{\psi}} \\ \hat{\boldsymbol{b}} \end{pmatrix}. \tag{B2}$$

Now let $C = N_f D_L^{-1/2} Q^T K \in \mathbb{R}^{M \times N}$. The singular value decomposition of the real matrix C is denoted

$$C = S\Omega R^T,$$

where $S \in \mathbb{R}^{M \times M}$ and $R \in \mathbb{R}^{N \times N}$ are orthogonal matrices and $\Omega = \mathrm{diag}(\omega_1, \ldots, \omega_M)$ is an $\mathbb{R}^{M \times N}$ matrix whose off-diagonals are zero and whose diagonal contains the M real, positive singular values of C. Hence (B2) can be written as

$$\frac{d}{dt} \begin{pmatrix} \hat{\boldsymbol{\psi}} \\ \hat{\boldsymbol{b}} \end{pmatrix} = \begin{bmatrix} 0 & \alpha(t) S\Omega R^T \\ -R\Omega^T S^T & 0 \end{bmatrix} \begin{pmatrix} \hat{\boldsymbol{\psi}} \\ \hat{\boldsymbol{b}} \end{pmatrix}.$$

Transforming again with $\tilde{\boldsymbol{\psi}} = S^T \hat{\boldsymbol{\psi}}$ and $\tilde{\boldsymbol{b}} = R^T \hat{\boldsymbol{b}}$ yields the system of (forced) harmonic oscillators

$$\frac{d}{dt} \begin{pmatrix} \tilde{\boldsymbol{\psi}} \\ \tilde{\boldsymbol{b}} \end{pmatrix} = \begin{bmatrix} 0 & \alpha(t)\Omega \\ -\Omega^T & 0 \end{bmatrix} \begin{pmatrix} \tilde{\boldsymbol{\psi}} \\ \tilde{\boldsymbol{b}} \end{pmatrix}. \tag{B3}$$

Expressed in terms of components, the above system becomes

$$\frac{d^2}{dt^2}\tilde{\psi}_i = -\alpha(t)\omega_i^2\tilde{\psi}_i + \dot{\alpha}(t)\omega_i\tilde{b}_i, \qquad i = 1,\ldots,M, \qquad (B\,4)$$

$$\frac{d^2}{dt^2}\tilde{b}_i = -\alpha(t)\omega_i^2\tilde{b}_i, \qquad i = 1,\ldots,M, \qquad (B\,5)$$

$$\frac{d^2}{dt^2}\tilde{b}_i = 0, \qquad i = M+1,\ldots,N. \qquad (B\,6)$$

To summarize, let $X = QD_L^{-1/2}S \in \mathbb{R}^{M\times M}$ and $Y = \frac{1}{N_f}R \in \mathbb{R}^{N\times N}$. The columns of X and Y, denoted $(X_1,\ldots,X_M)$ and $(Y_1,\ldots,Y_N)$, respectively, represent the normal modes of $\boldsymbol{\psi}$ and $\boldsymbol{b}$. Then the normal mode decomposition

$$\boldsymbol{\psi} = X\tilde{\boldsymbol{\psi}}, \qquad \boldsymbol{b} = Y\tilde{\boldsymbol{b}}, \qquad (B\,7)$$

yields a system of M independent systems (B 4)–(B 5), plus the $N-M$ trivial dynamics (B 6).

REFERENCES

ARNOLD, V. I. 1989 *Mathematical methods of classical mechanics*, 2nd edn. Springer-Verlag.

BÜHLER, O. & HOLMES-CERFON, M. 2011 Decay of an internal tide due to random topography in the ocean. *J. of Fluid Mech.* **678**, 271–293.

GRISOUARD, N., STAQUET, C. & PAIRAUD, I. 2008 Numerical simulation of a two-dimensional internal wave attractor. *J. Fluid Mech.* **614**, 1–14.

HAIRER, E., LUBICH, C. & WANNER, G. 2006 *Geometric numerical integration : Structure-preserving algorithms for ordinary differential equations*. Berlin: Springer.

HAZEWINKEL, J., VAN BREEVOORT, P., DALZIEL, S. B. & MAAS, L. R. M. 2008 Observations on the wavenumber spectrum and evolution of an internal wave attractor. *J. Fluid Mech.* **598**, 373–382.

HOLM, D. D., MARSDEN, J. E. & RATIU, T. S. 2002 The Euler-Poincaré equations in geophysical fluid dynamics. In *Large-Scale Atmosphere-Ocean Dynamics II* (ed. I. Roulstone & J. Norbury), pp. 251–300. Cambridge University Press.

JOHN, F. 1941 The Dirichlet problem for a hyperbolic equation. *American Journal of Mathematics* **63**, pp. 141–154.

KOPECZ, S. 2006 Fractal internal wave patterns in a tilted square. Unpublished Report, Kassel University, http://www.nioz.nl/kopecz.

LAM, F.-P. A. & MAAS, L. R. M. 2008 Internal wave focusing revisited; a reanalysis and new theoretical links. *Fluid Dynam. Res.* **40** (2), 95–122.

LEIMKUHLER, B. J. & REICH, S. 2004 *Simulating Hamiltonian dynamics*. Cambridge University Press.

LIGHTHILL, J. 1996 Internal waves and related initial-value problems. *Dynamics of Atmospheres and Oceans* **23**, 3 – 17.

MAAS, L. R. M. 2005 Wave attractors: linear yet nonlinear. *Internat. J. Bifur. Chaos* **15** (9), 2757–2782.

MAAS, L. R. M. 2009 Exact analytic self-similar solution of a wave attractor field. *Physica D: Nonlinear Phenomena* **238** (5), 502 – 505.

MAAS, L. R. M., BENIELLI, D., SOMMERIA, J. & LAM, F.-P. A. 1997 Observation of an internal wave attractor in a confined, stably stratified fluid. *Nature* **388**, 557–561.

MAAS, L. R. M. & LAM, F.-P. A. 1995 Geometric focusing of internal waves. *J. Fluid Mech.* **300**, 1–41.

MCEWAN, A. D. & ROBINSON, R. M. 1975 Parametric instability of internal gravity waves. *Journal of Fluid Mechanics* **67** (04), 667–687.

MCLACHLAN, R. I. 1995 Symplectic integration of hamiltonian wave equations. *Numerische Mathematik* **66** (1), 465–492.

Morrison, P. J. 1998 Hamiltonian description of the ideal fluid. *Rev. Mod. Phys.* **70** (2), 467–521.

Ogilvie, G. I. 2005 Wave attractors and the asymptotic dissipation rate of tidal disturbances. *J. Fluid Mech.* **543**, 19–44.

Olver, P. J. 1986 *Applications of Lie groups to differential equations*. New York: Springer-Verlag.

Salmon, R. 1998 *Lectures on Geophysical Fluid Dynamics.*. Oxford University Press.

Swart, A., Sleijpen, G. L. G., Maas, L. R. M. & Brandts, J. 2007 Numerical solution of the two-dimensional Poincaré equation. *J. Comput. Appl. Math.* **200** (1), 317–341.

Whitham, G. B. 1974 *Linear and nonlinear waves*. New York: Wiley.